Bound states and Pb 6*p* orbital selectivity in orthorhombic $CsPbI_3$ bulk crystal

L. Craco,[1,2] B. Oliveira,[1] S. S. Carara,[1] P. H. Z. de Arruda,[1] and S. Leoni[3]
[1]*Institute of Physics, Federal University of Mato Grosso, 78060-900 Cuiabá, MT, Brazil*
[2]*Leibniz Institute for Solid State and Materials Research Dresden, D-01069 Dresden, Germany*
[3]*School of Chemistry, Cardiff University, Cardiff CF10 3AT, United Kingdom*

(Received 27 August 2025; revised 19 November 2025; accepted 9 February 2026; published 6 March 2026)

We investigate the orbital-selective electronic structure of orthorhombic $CsPbI_3$ bulk perovskite using density functional theory combined with dynamical mean-field theory. By considering realistic values of the on-site Coulomb repulsion and spin–orbit coupling, we reveal characteristic features in the spectral functions of the active Pb-6*p* orbitals, including the formation of spin–orbit–induced low-energy bound states. Our results further demonstrate that electron doping drives a substantial reconstruction of the electronic structure, leading to Pb-orbital selectivity. These findings provide microscopic insights into the interplay between electronic plus spin–orbit interactions and doping in orthorhombic $CsPbI_3$ crystal, offering a framework to understand its correlated electronic state.

DOI: 10.1103/d6yp-lf91

I. INTRODUCTION

Since the seminal proposal of organometal lead halide perovskites as visible-light sensitizers for photovoltaic solar cell applications [1], a plethora of studies on three-dimensional (3D) halide perovskites (HPs) have been performed in the last two decades. The HPs are structured as corner-sharing octahedra with the formula ABX_3, where A corresponds to a monovalent cation metal (K, Rb, Cs) or organic molecular cation [methylammonium (*MA*), formamidinium (*FA*)], B is a column IV element (Ge, Sn, Pb), and X is a halogen anion (Cl, Br, I) [2]. Based on experimental and theoretical studies, the HPs are now considered as a promising class of 3D semiconducting materials in view of their ability to offer a range of tunable band gaps, making them attractive candidates for optoelectronic applications, including solar cells, light-emitting diodes, lasers, and photodetectors [3] as well as for high-temperature thermoelectric applications [4,5]. Importantly, the hybrid perovskite photovoltaic devices have efficiencies similar to those made using Si- or CdTe-based technologies for extant photovoltaic applications [6–8]. However, unavoidable stability issues, such as photodegradation under irradiation and decomposition to a yellow phase [9,10] are open issues that needed to be sorted out in view of using HP as materials for photovoltaics [9]. Moreover, apart from solar cell applications, organic, inorganic, and hybrid (organic-inorganic) HPs [11,12] have been considered as candidates for resistive switching memory devices [13]. In these systems, hysteresis loops are observed in current-voltage (I–V) characteristics [14–16], which might be associated with ion migration [17] or other mechanisms [14]. As pointed out in Ref. [18], mixed ionic-electronic conductivity can be detrimental to solar cell operation but it might be relevant in resistive switching [19], adding the lead HPs into the memristive family for future technologies [14,20].

HPs are mostly direct band gap semiconductors that exhibit sharp absorption onsets [21]. Among this family of materials, the most efficient solar cell materials are the organic–inorganic Pb-containing HPs, with power conversion efficiency close to 27% [22], although a theoretical limit of 31% has been postulated in Refs. [1,23]. Particularly interesting in this context are the inorganic cesium lead halide systems ($CsPbX_3$, $X = \mathrm{Br}, \mathrm{I}$), which are now considered as promising candidates for solar cell applications because of their thermal stability [24].

On general grounds, the cubic perovskite structure is known to exhibit various possible structural phase transitions, which fall in two main categories: ferroelectric distortions, where the B atom in the ABX_3 lattice structure is displaced within its surrounding octahedron, and antiferroelectric distortions, in which the octahedra rotate at about multiple axes [25]. Depending on the type of displacement, for example, along the [001] cubic axis, or along the [110] and [111] directions, the resulting symmetry becomes, respectively, tetragonal, orthorhombic, or rhombohedral. Thus, for rotation-type phase instabilities, while rotation about a cubic axis leads to a tetragonal structure, rotation on two orthogonal axes leads to an orthorhombic phase [25], which could show some octahedral tilt instabilities [26].

Presently, the most efficient alloy engineering techniques to enhance structural phase stability include substitution on the A site of the ABX_3 crystal lattice, aiming to stabilize the photoactive black perovskite polymorph [6,27,28], while substitution on the halide site can be used to tune the one-particle band gap [29]. Of note is the fact that the HPs undergo structural phase transitions as a function of temperature (T) [30],

which gives rise to octahedral tilt instabilities as explained geometrically by the Goldschmidt tolerance factor [26]. Hence, within the framework of HPs structural phase transitions, the high-T cubic α phase (space group $Pm\bar{3}m$) may show structural transitions either to a tetragonal ($P4/mbm$) β phase with in-phase tilts [31] or to a $I4/mcm$ β phase with out-of-phase tilts [32]. Additionally, both inorganic and hybrid lead HPs show the emergence of two orthorhombic γ phases, with different tiltings as compared to nonorthorhombic structural phases [9,33–35]. Interestingly, $CsPbI_3$ and $CsSnI_3$ [36] also exhibit a photoinactive, nonperovskite (yellow) δ-phase polymorph, which consists of one-dimensional (1D) chains of face-sharing octahedra [9,33,34,37], indicating the coexisting stable or possibly metastable [32,38] phases in this material class. While the δ phase is the most likely thermodynamic equilibrium phase at low T [6,27,39], the technologically relevant phases include predominantly the perovskite series.

Bulk $CsPbI_3$ crystals observed using synchrotron powder diffraction showed a black perovskite cubic α phase [9,40] as the high-T stable phase. On cooling, this α phase changes into a black perovskite β phase around 260 °C [9]. Further cooling transforms this phase into a black perovskite γ phase around 175 °C [9]. This γ phase was reported to have symmetry of *Pbnm* (*Pnma* in the standard setting) [9,41]. The band gap for the α phase is about 1.73 eV [42,43], while the band gap for the β phase was found to be close to 1.68 eV [44] in $CsPbI_3$ films. Finally, the band gap for the two γ phases is close to 1.96 eV [45]. It should also be noted that this latter phase is metastable [38,46], particularly when it is left for a few days under ambient conditions, making it less attractive for solar cell applications. However, based on extant studies reporting the physical properties of the different structural phases, here we explore the electronic structure of γ-$CsPbI_3$ computationally using density functional theory (DFT) and DFT plus dynamical mean-field theory (DFT + DMFT) calculations. We reveal the important role played by lattice crystal-field splittings, multi-orbital (MO) electron-electron interactions, spin-orbit coupling (SOC), and electron-doping effects on the Pb-6p orbital texture of the orthorhombic structural phase of $CsPbI_3$ solar cell semiconductor. These are among the different factors that could influence the band gap size of HPs. More precisely, for III-V semiconductors, the SOC may change the one-particle band dispersion in the vicinity of the valence-band maximum and the conduction-band minimum [47,48], inducing a band gap reduction that can reach 0.3 eV according to Ref. [49]. The band gap can also be affected by lattice distortions, many-particle electron-electron interactions, and alloy disorder, resulting in changes in the DFT electronic structure. Thus, to unravel the nature of the underlying many-body state of Pb-containing HP semiconductors, it is essential to explore the role played by different factors while using theoretical state-of-the-art capabilities.

Before addressing the fundamental principles underlying the electronic structure reconstruction induced by MO electron–electron interactions [50,51] and SOC effects [48,52–55] in γ–$CsPbI_3$, it is important to emphasize that relativistic effects associated with SOC in HPs have been experimentally observed (see Ref. [56]) and extensively discussed in theoretical studies over the past few years [46–48,57–60]. Acting on the Pb-6p orbitals, SOC

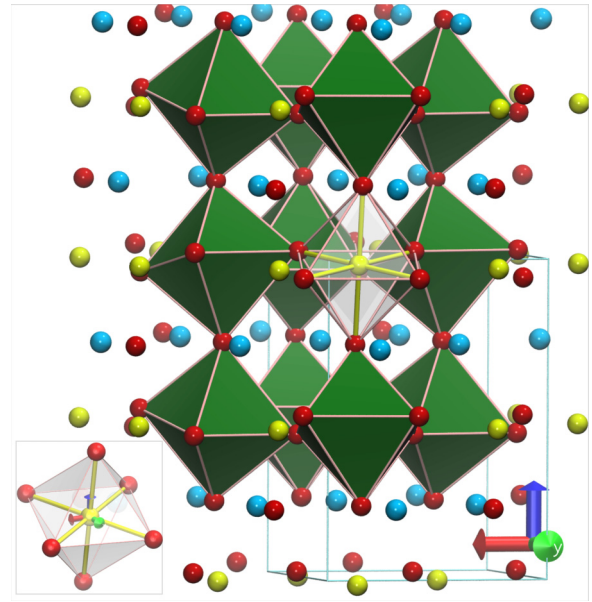

FIG. 1. Crystal structure of orthorhombic CsPbI3 (*Pnma* setting), emphasizing the octahedral coordination of Pb by I, as well as the tilted arrangement of corner-sharing octahedral (green polyhedra). Cs is blue, Pb yellow, and I is red. The unit cell is shown in the main panel. The inset shows the orientation of the octahedron with respect to Cartesian axes (origin on Pb).

enhances the band dispersion [57,61], which in turn reduces the one-particle band gap either by splitting the conduction-band states [46,48,59] or by forming antibonding states at the valence-band maximum [61]. These modifications pose challenges for describing the electronic structure of Pb-based HPs within conventional DFT approaches [46–48,62]. Nevertheless, previous works have successfully described many-body interactions using DFT + GW [50,63] and the DFT + DMFT [64] frameworks, demonstrating in the latter case the reliability of DFT + DMFT to broadband systems such as elemental Bi [52], topological insulators [53,65], cubic $CsPbI_3$ [51], and more recently to twisted bilayer and trilayer graphene [66]. To the best of our knowledge, however, studies considering the interplay of MO correlations and SOC remain scarce for the distorted structural phases of $CsPbI_3$ perovskite. Motivated thereby, we focus here on the reconstruction of the electronic structure of γ-$CsPbI_3$ driven by MO electron–electron interactions and SOC.

II. THEORY AND RESULTS

In this work, first-principles electronic structure calculations for γ-$CsPbI_3$ (see Fig. 1) were performed within DFT using the SIESTA code [67] (v4.1.5). Norm-conserving pseudopotentials of the Troullier-Martins type were employed, generated within the PBE (Perdew-Burke-Ernzerhof) [68] generalized gradient approximation (GGA) exchange–correlation functional. The valence electron configurations used in the pseudopotentials included semicore states for both Pb ($5d^{10}6s^26p^2$) and Cs ($5s^25p^66s^1$), while I was described with $5s^25p^5$. The plane-wave equivalent energy cutoff for the real-space mesh was set to 320 Ry and Brillouin zone

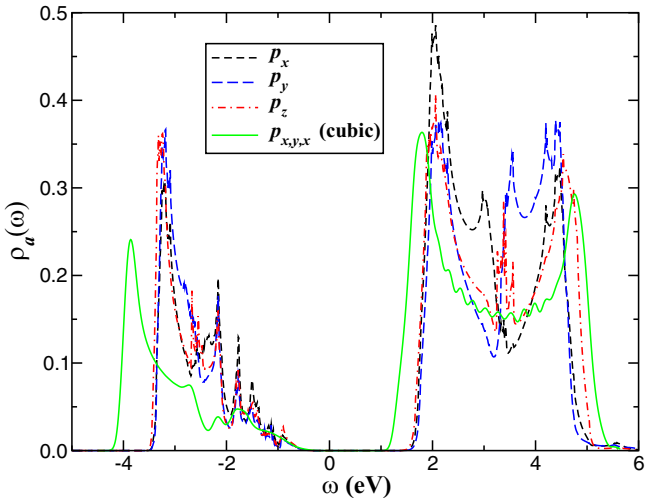

FIG. 2. Orbital-resolved DFT Pb-6p density of states (DOS) of orthorhombic $CsPbI_3$ bulk crystal. Notice the large bare bandwidth ($W \approx 8.5$ eV), the semiconducting band gap of ≈2.05 eV and the splitting of the Pb-6p orbitals because of octahedral tilted crystal-field effects. The DOS of the cubic phase obtained using the SIESTA code in Ref. [51] is shown for comparison.

sampling was carried out on a $10 \times 10 \times 10$ Monkhorst-Pack grid [69]. The crystal structure was fully relaxed in both lattice parameters and atomic coordinates using the conjugate-gradient (CG) algorithm until forces and stresses fell below the convergence thresholds of 0.002 eV/Å and 0.1 GPa. The converged DFT electronic structure was interfaced with Wannier90 (v3.0.0) [70] to construct maximally localized Wannier functions (MLWFs) for the target bands. Initial projections were chosen as iodine 5p orbitals and lead 6s and 6p orbitals, providing an optimal starting guess for the localization procedure. Fifty two Wannier functions were disentangled from a total of 62 bands, using an inner energy window maximum of 0.5 eV and an outer energy window maximum of 5.0 eV relative to the Fermi level. Wannierization convergence was monitored via the spread functional, with final orbital spreads in the range 2.09–3.15 Å^2 per orbital.

In Fig. 2, we display our results for the orbital-resolved DFT Pb-6p density of states (DOS), $\rho_a(\omega) = -\frac{1}{\pi}\mathrm{Im}G_a(\omega)$ of a given orbital $a = x, y, z$ and spin σ, revealing how the Pb-6p states of γ-$CsPbI_3$ split because of crystal-field effects arising from octahedral tilts. Also noteworthy is the large band gap that spans the Fermi level ($E_F = \omega = 0.0$ eV) in this broadband semiconductor. This intrinsic band gap behavior is known to be relevant for HP solar cell applications, enabling higher optical absorption [5]. Based on our DFT calculation, the band gap for γ-$CsPbI_3$ is approximately 2.05 eV, which is in good agreement with the 1.96 eV value found in Ref. [45]. Moreover, our results for the partial DOS are also consistent with that reported for $\alpha-CsPbI_3$ [5,51], showing that the conduction band minimum is composed mostly by the 6p orbitals of Pb. However, the valence band maximum is originated by the 5p orbitals of iodine atom, with clear Pb-I hybridization, which give rise to bonding-antibonding bands. On the other hand, and different from the α phase the octahedral tilt increases the Pb-I overlap, which in turn increases the one-particle band gap, as shown in Fig. 2. As seen in this figure, because of band narrowing, the conduction band states of γ-$CsPbI_3$ are pushed up in energy by approximately 0.5 eV. Thus, apart from Pb-6p-orbital splitting, an important message in Fig. 2 is the distortion-induced weak electron localization in γ-$CsPbI_3$ as compared to cubic $CsPbI_3$. Also interesting in this direct comparison between the threefold degenerated α-phase DOS with the γ one is the spectral weight of the bonding band below E_F, which increases because of lattice distortion. Importantly, enhancement of valence band spectral weight in γ-$CsPbI_3$ with an orbital occupancy per spin close to 0.25 (i.e, total Pb-6p band filling $n_{DFT} = 1.5$) would increase electron correlation effect in this phase as compared to the α phase, placing γ-$CsPbI_3$ naturally into a quarter-filled correlated semiconducting [71] regime as shown below.

Based on DFT, the one-electron part at each atomic Pb 6p orbital of γ-$CsPbI_3$ bulk crystal is $H^0 = \sum_{\mathbf{k},a,\sigma} \epsilon_a(\mathbf{k}) c^\dagger_{\mathbf{k},a,\sigma} c_{\mathbf{k},a,\sigma} - \mu \sum_{i,a,\sigma} n_{i,a,\sigma}$, where $a = x, y, x$ label the (diagonalized in orbital basis) 6p bands as in Fig. 2. In the usual notation, within the three-orbital problem of γ-$CsPbI_3$, $c^\dagger_{i,a,\sigma}$ ($c_{i,a,\sigma}$) are creation (annihilation) operators at site i of a electrons with spin σ and $n_{i,a,\sigma} = c^\dagger_{i,a,\sigma} c_{i,a,\sigma}$. $\epsilon_a(\mathbf{k})$ is the one-electron band dispersion, which encodes details of the actual band structure and μ is the chemical potential. Local many-particle interactions in $CsPbI_3$ bulk crystal are encoded in H^{int} [51], which reads $H^{int} = U \sum_{i,a} n_{i,a,\uparrow} n_{i,a,\downarrow} U' \sum_{i,a\neq b} n_{i,a} n_{i,b} - J_H \sum_{i,a\neq b} \mathbf{S}_{i,a} \cdot \mathbf{S}_{i,b}$, where $U' \equiv U - 2J_H$ with U (U') being the intra- (inter) orbital Coulomb repulsion and J_H is the Hund's rule coupling. To treat the dynamical many-particle effects produced by U, U', J_H, we use DFT + DMFT [64] as an approximation to the many-body Hamiltonian $H^{MO} = H^0 + H^{int}$ of γ-$CsPbI_3$. Finally, to investigate the role played by the SOC [57,59,63] within our formulation, we considered, for the sake of simplicity, only the local component of this quantum interaction [72], which can be treated exactly within DMFT [73,74]. Thus, similar to Refs. [51–53], on atomic Pb, the local SO Hamiltonian reads $H^{SO} = \lambda \sum_{i,a} (c^\dagger_{i,a,\uparrow} c_{i,a,\downarrow} + \mathrm{H.c.})$ with λ being the SOC, which could reach values up to 1.21 eV for $CsPbI_3$ crystal [57]. Noteworthy, similar to the U, U', and J_H, the SOC is taken as model parameter in our description given the uncertainty in its precise value [48,57]. Physically, H^{SO} acts as a spin-flip term [74] and locally mixes the 6p_a spin states of Pb. As in Ref. [51], here we evaluate the many-particle Green's functions $G_{a,\sigma}(\omega, \mathbf{k}) = [\xi_{a,\sigma}(\omega) - \epsilon_a(\mathbf{k}) - \delta_a \frac{\lambda^2}{\xi_{a,\sigma}(\omega)}]^{-1}$, where $\xi_{a,\sigma}(\omega) \equiv \omega + \mu + i\eta - \Sigma_{a,\sigma}(\omega + i\eta)$, of the model Hamiltonian $H = H^0 + H^{int} + H^{SO}$ for γ-$CsPbI_3$ crystal using the DFT + DMFT approximation [64]. Similar to Ref. [51], here we use MO iterated-perturbation theory (MO-IPT) as impurity solver [75] when treating the MO problem of γ-$CsPbI_3$ self-consistently. It is noteworthy that similar interpolation scheme for the local self-energy has been used to investigate correlation effects in two-dimensional topological insulators [65], and very recently for twisted bilayer and trilayer graphene [66]. The MO-IPT is known to be numerically very efficient and self-energies [$\Sigma_{a,\sigma}(\omega)$] can be computed accurately at both small and large frequencies.

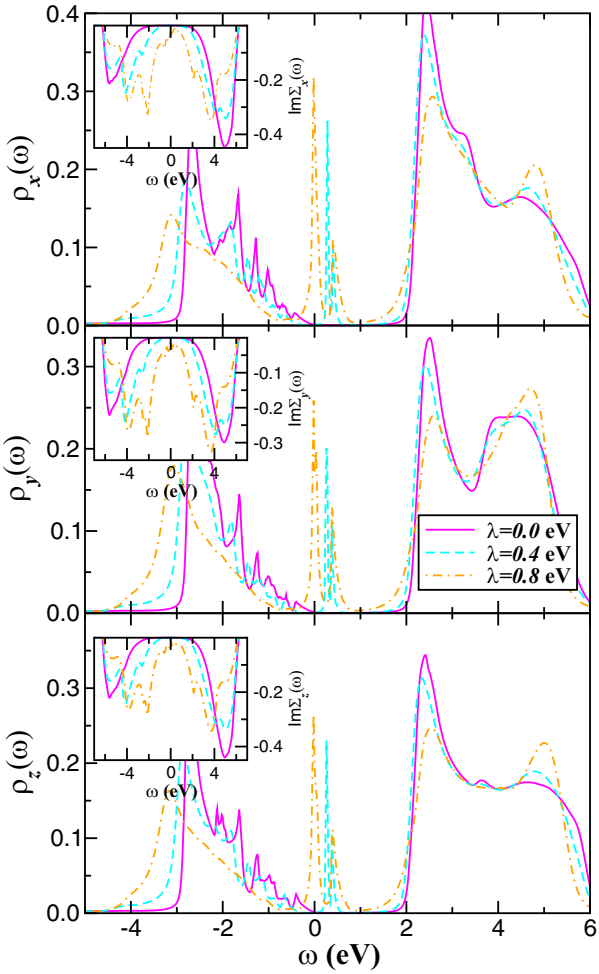

FIG. 3. Effect of spin-orbit coupling λ on the Pb-correlated DFT + DMFT ($U = 9.0$ eV) orbital-resolved DOS of orthorhombic $CsPbI_3$ bulk crystal. Important features to be seen are the low-energy bound states near E_F below and the evolution of upper Hubbard bands near to 5.0 eV above E_F as well as the changes in the valence band shoulder features with increasing λ. Also noteworthy is the frequency dependence of the self-energy imaginary parts in the insets.

Given the complexity in $CsPbI_3$ with three ($a = x, y, z$) $6p$ orbitals, these are particularly attractive features to treat electron-electron plus SO interactions in correlated broadband semiconductors [71].

In Fig. 3, we show the reconstructed one-particle DOS of γ-$CsPbI_3$ obtained using $U = 9.0$ eV [76], $J_H = 0.7$ eV and three different values of λ, which in Pb-containing materials can reach values between 0.68 to 1.21 eV [48,57]. Let us first look at the role played by electron interactions in the orbital-resolved local DOS in the $\lambda = 0.0$ eV regime. Similar to Ref. [51], an electronic reconstruction from the bare DFT semiconductor to a correlated semiconducting state occurs because of dynamical transfer of spectral weight in a regime where correlation to bandwidth ratio (U/W) is close to one. Looking closely at our DFT + DMFT orbital-resolved results for $\lambda = 0.0$ eV, a remarkable aspect stands out: $\mathrm{Im}\Sigma_a(\omega)$ vanishes in the gap region, instead of having a pole, as would occur in a Mott insulator. This aspect is reminiscent of a Kondo insulator, where the gap arises due to combined effects of electronic correlations and interband hybridization. Thus, the correlated semiconducting behavior [71] of γ-$CsPbI_3$ in absence of SOC is that of a Kondo-like correlated insulator [75,77].

For clarity, it is worth recalling that Kondo insulators are correlated systems [78] whose excitations and normal-state properties are adiabatically connected to those of noninteracting semiconductors [79]. They can thus be regarded as an analytically continued version of conventional band insulators, but with significant electronic correlations persisting above the one-particle band gap. In such systems, when the band filling deviates slightly from its commensurate value, a coherent Kondo cloud emerges near E_F, giving rise to a metallic Fermi-liquid (FL) state in the absence of disorder. This behavior is evident in the orbital-resolved self-energies at $\lambda = 0.0$ eV, where correlation effects appear as peak-like structures in the imaginary part of the self-energy above the band gap (see insets of Fig. 3), revealing the underlying Kondo-like correlated character of the system. Consequently, since γ-$CsPbI_3$ is Kondo-correlated, spectral weight redistribution triggered by additional perturbation, such as SOC, can drive the Kondo-like insulating to a bound state phase, as illustrated in the main panels of Fig. 3. Specifically, Fig. 3 shows how the Pb orbital-resolved DOS is reconstructed when electronic correlations are combined with SO interaction. As reported in Ref. [51] and consistent with Ref. [59], SOC splits the Pb conduction-band states into two branches, giving rise to bound states near E_F, similar to those reported for Bi-chalcogenide topological insulators [53]. Another striking feature in Fig. 3 is the large-scale reconstruction of the electronic structure with increasing SOC: While conduction-band-edge states are dynamically transferred to higher energies, enhancing the spectral weight of the upper Hubbard bands (UHB), the valence bonding band is significantly reshaped, reinforcing the incoherent character of the lower Hubbard band (LHB). Equally important are the SOC-driven modifications in the imaginary part of the self-energy. The transverse-field or spin-flip nature of H^{SO} induces the formation of bound states through local spin fluctuations [73], thereby reducing the band gap at $\lambda = 0.0$ eV.

Taken together, the results in Fig. 3 at finite λ reveal the emergence of low-energy in-gap states near E_F. What underlies the features observed in Fig. 3? In many-particle systems, strong scattering among carriers, split by specific crystal-field effects, produces two key consequences: (i) orbital-dependent shifts of the bands, driven by the frequency dependence of the self-energies (see Fig. 3, insets), and (ii) renormalized scattering rates arising from sizable U, U', J_H, and λ, which induce significant spectral weight transfer over broad energy scales, from high to low energies. The latter effect modifies the spectral lineshape through local spin fluctuations [73], as also evident in Fig. 3. Consequently, broadening-induced changes in the DOS at finite λ, compared to the SOC-free case, lead to a tunable reduction of the semiconducting band gap [51], with enhanced low-energy spectral features in both valence and conduction states appearing near E_F. On the microscopic level, scattering processes resulting from the coexistence of local Coulomb correlations and SOC drive a pronounced reconstruction of the low-energy spectral functions, whose

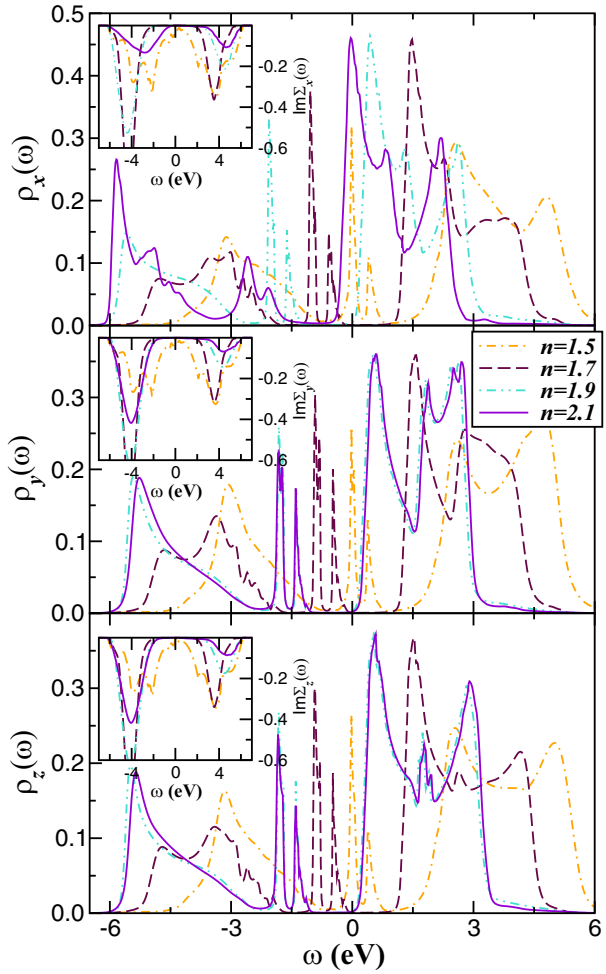

FIG. 4. Orbital-resolved electronic structure reconstruction of orthorhombic $CsPbI_3$ with increasing the total band filling n of the Pb shell obtained for $U = 9.0\,\text{eV}$ and $\lambda = 0.8\,\text{eV}$. An important feature to be observed is the transfer of spectral weight from the conduction to the lower Hubbard bands and the reemergence of the Kondo-like correlated insulating state as shown by the ω dependence of self-energy imaginary parts in the insets.

signatures should be accessible in future experiments. Importantly, the emergent electronic state in γ-$CsPbI_3$ is coherent at small λ but evolves into an incoherent state at $\lambda = 0.8\,\text{eV}$, as indicated by the ω dependence of the self-energy imaginary parts (Fig. 3, insets). This implies that the Kondo-like insulator identified at $\lambda = 0.0\,\text{eV}$ in γ-$CsPbI_3$ is entirely suppressed by strong scattering rates, reflecting the fundamental breakdown of Kondo coherence under sizable SOC.

To further elucidate the electronic structure reconstruction of γ-$CsPbI_3$ bulk crystal, Fig. 4 shows the effect of increasing the total Pb-band filling n. This analysis is motivated by earlier studies on doping [80] or alloy [81] engineering metal HPs as well as by the fact that, within the DFT + DMFT framework, electron doping cannot be described as a simple rigid shift of the bare DFT bands; instead, it must be treated self-consistently. Understanding the impact of doping on the reconstructed electronic state is therefore essential. Although several theoretical and experimental studies have already addressed related aspects, the generic emergence of reconstructed electronic states and their instability toward metallic behavior (whether FL or not) in other correlated systems highlights the relevance of this issue. Our goal here is to exploit the strengths of MO correlated electronic structure calculations to model and analyze how increasing the total band filling modifies the electronic spectra of γ-$CsPbI_3$. Based on our explicit results, we also propose a set of predictions that could be tested in future tunneling, spectroscopic, and transport experiments, or by tuning the Fermi level position [82] through controlled changes in the chemical potential μ.

Figure 4 represents the modifications in the correlated DOS (main panels) and in the imaginary part of the self-energy (insets), computed for $U = 9.0\,\text{eV}$, $J_H = 0.7\,\text{eV}$, and $\lambda = 0.8\,\text{eV}$, as the total band filling ($n = n_{DFT} + \delta$) of electron-doped γ-$CsPbI_3$ is gradually increased. A remarkable result is that orbital selectivity emerges already at small $\delta(\approx 0.2)$, highlighting the sensitivity of correlated, wide-band systems to electron addition. At this doping level, all SOC-induced bound states appear below E_F, confirming the tunability [47,48] of such states in this material family. As δ increases further, around 0.4, the orbital-selective behavior becomes more pronounced, with LHBs being more clearly visible at binding energies below 4.5 eV. The origin of these orbital-selective features lies in the interplay of crystal-field effects, electron-electron interactions and SOC acting on the bare DFT electronic structure. Two main consequences follow: (i) orbital-dependent shifts of the Pb-6p states relative to each other, arising from Hartree contributions to the static part of the self-energies, and (ii) dynamical effects associated with sizable U, U', J_H, and λ, which promote large-scale spectral weight transfer across wide energy ranges upon doping. This mechanism explains the orbital-dependent modifications of the one-particle DOS and self-energies observed in Fig. 4. As a result, electron-doped γ-$CsPbI_3$ exhibits orbital-selective narrow bound states below E_F. The interplay of orbital selectivity and strong spectral weight redistribution constitutes a robust fingerprint of the correlated electronic state in this broadband perovskite, warranting future experimental verification.

As seen in Figs. 3 and 4, bound states and relativistic [83] SOC are deeply interconnected in correlated semiconductors. The SOC modifies the band dispersion, splitting conduction- or valence-band edges into distinct branches. As shown in Figs. 3 and 4, this reconstruction can confine electronic states near E_F, giving rise to low-energy bound states. Such states are not mere artifacts of electronic structure, but signatures of strong interactions between relativistic effects and electron correlations. In correlated semiconductors, the appearance as localized in-gap features, influencing transport response (see Fig. 5). In this sense, SOC-induced bound states provide a microscopic link between SO effects and emergent novel electronic behavior. Thus, carrier's self-trapping [84], which might be induced in a system with SOC interactions, can be taken as a manifestation of the strong coupling between orbital and spin degrees of freedom in correlated semiconducting materials. The SOC can increase the localization tendency by splitting orbital or band states [48,57] and generating bound states near the band edges, thereby reducing the mobility of itinerant carriers. Here, local spin fluctuations act as a local scattering channel that disrupt coherent motion,

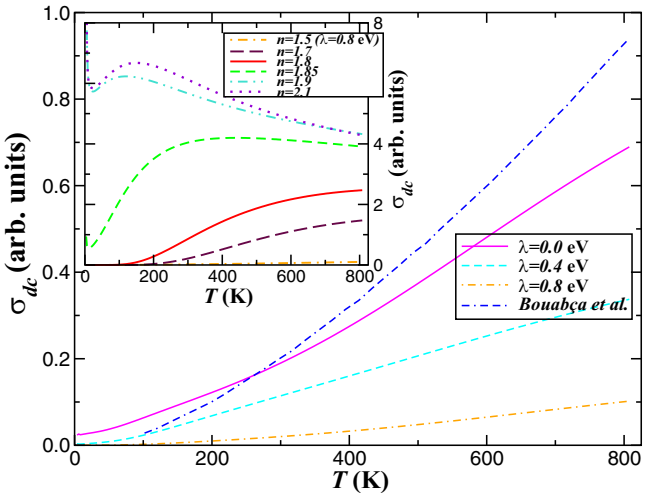

FIG. 5. Electrical conductivity vs temperature of pure (main panel) and electron-doped (inset) γ-$CsPbI_3$ semiconductor obtained using the DFT + DMFT spectral functions for different spin-orbit couplings (main panel) and total Pb-6p band fillings (inset). The dc-conductivity curve reported in Ref. [4] (normalized to 0.93 at 800 K) is shown for comparison in the main panel. Notice the good qualitative agreement between this curve and that obtained for $\lambda = 0.0$ eV. Also interesting in the inset is the clearly visible doping dependence of $\sigma_{dc}(T)$ at fixed λ.

reinforcing the confinement of charge carriers into self-trapped states. Importantly, self-trapping driven by relativistic [48,61] or spin-mediated effects provides a microscopic mechanism for unconventional insulating behavior in materials where a purely band-like description would predict semiconducting conduction. As revealed in Figs. 3 and 4, these processes highlight the delicate balance between coherence and localization, showing how SOC-induced local transverse-field [74] spin fluctuations can cooperate to reshape the low-energy electronic structure.

Building on earlier studies that highlight the potential of HPs for high-temperature thermoelectric applications [4,5], we now examine the T dependence of the dc conductivity and relate it to the orbital-reconstruction scenario discussed above. Given the correlated spectral functions $A_{a,\sigma}(\mathbf{k},\omega) = -\frac{1}{\pi}\mathrm{Im}G_{a,\sigma}(\mathbf{k},\omega)$, the (static) dc conductivity $[\sigma_{dc}(T)]$, computed within the DMFT formalism [85,86], can be expressed as $\sigma_{dc}(T) = \frac{2\pi e^2}{\hbar\mathcal{V}} v^2 \sum_{a,\sigma} \int d\epsilon A^{(0)}_{a,\sigma}(\epsilon) \int d\omega A^2_{a,\sigma}(\epsilon,\omega)[-f'(\omega)]$. In this expression, $A^{(0)}_{a,\sigma}(\epsilon)$ is the bare DFT DOS of the a orbitals with spin-σ (Fig. 2), $\mathcal{V}$ is the unit-cell volume, and $f(\omega)$ is the Fermi function. As in Ref. [52], the approximation made here is to ignore the $\mathbf{k}$ dependence of electron's velocity $v_{\mathbf{k},a}$. In this situation, following Saso *et al.* [87], we approximate $v_{\mathbf{k},a}$ by an effective, k-independent carrier velocity (v) for the Pb-6p orbitals. Importantly, Refs. [87] and [88] have shown that this assumption works well for numerical computations of $\sigma_{ac}(\omega)$ for Kondo insulators (FeSi and YbB_{12}), V_2O_3 and Fe-pnictide superconductors, supporting our approximation in $\sigma_{dc}(T)$ above. Furthermore, the same approximation has been successfully employed in studies of thermoelectric transport in p- and d-band systems [89], consistently yielding qualitative good agreement between theory and experiment.

In Fig. 5, we present the T dependence of the electrical conductivity $\sigma_{dc}(T)$, computed using the $T = 0$ K orbital-resolved DFT + DMFT spectral functions for both the undoped (main panel) and electron-doped (inset) γ-$CsPbI_3$ semiconductor, using fixed $U = 9.0$ eV together with the SOC and doping values adopted in Figs. 3 and 4. As shown in the main panel of Fig. 5, the DFT + DMFT results for the parent compound display an increase in conductivity with temperature, consistent with the intrinsic semiconducting character of γ-$CsPbI_3$. Notably, the $\sigma_{dc}(T)$ curve at $\lambda = 0.0$ eV shows good qualitative agreement with earlier results for $CsPbI_3$ [4], supporting the validity of the approximations employed in our calculations. A key observation, however, is that $\sigma_{dc}(T)$ decreases once SOC is included. This occurs because the SOC-induced bound states [90] are confined at low energies, reducing the thermally activated itinerancy of charge carriers. Such confinement may be linked to the carrier self-trapping recently reported in the two-dimensional hybrid perovskite $(BA)_2(MA)_2Pb_3I_{10}$ [84]. Interestingly, this localization is lifted upon electron doping, as illustrated in the inset of Fig. 5, where the dc conductivity is restored with increasing $\mathrm{Pb} - 6p$ band filling n. This indicates that SOC-driven weak localization can be overcome by doping, paving the way for novel states of quantum matter. Another striking feature in the inset is the abrupt shift from a correlated semiconducting state to a metal at $n_{=}1.85$. Overall, our results suggest that the interplay between SOC-induced local spin fluctuations [74] and electron doping enables low-T itinerancy by opening a metallic channel within the correlated semiconducting background. Without this mechanism, γ-$CsPbI_3$ would remain a MO Kondo-like correlated insulator [53] down to the lowest temperatures. Thus, our DFT + DMFT analysis captures the emergence of metallicity, or equivalently, the suppression of self-trapping [84], as a function of band filling in this correlated p-band semiconductor.

In order to shine microscopic insights on the electronic structure reconstruction derived above and its possible link to current-voltage (I–V) characteristic of γ-$CsPbI_3$ memristor [91], in Fig. 6 we present our results computed using the total DFT + DMFT DOS corresponding the different λ (main panel) and n (inset) values considered, respectively in Figs. 3 and 4. As already pointed out in Ref. [51], within the wideband limit of the left (L) and right (R) electrodes, the current formula for a tunneling experiment reads $I = \frac{2e}{\hbar}\sum_\alpha \int d\omega\, \tilde{\Gamma}(\omega)\{f_L(\omega) - f_R(\omega)\}\rho_{total}(\omega)$ [92,93], where $\tilde{\Gamma}(\omega) = \Gamma_L(\omega)\Gamma_R(\omega)/\Gamma(\omega)$ with $\Gamma_\alpha(\omega) = \pi\sum_k |t^\alpha_k|^2\,\delta(\omega - \varepsilon_{k\alpha})$ being the coupling strength between electrode α and the central region [94], and $\Gamma(\omega) = \Gamma_L(\omega) + \Gamma_R(\omega)$. $f_\alpha(\omega) = 1/(e^{\beta(\omega-\mu_\alpha)} + 1)$ and $\rho_{total}(\omega)$ are, respectively, the Fermi function of the electrode α and the total DOS of the Pb-6p channel of γ-$CsPbI_3$. Moreover, for simplicity, we assume a symmetric voltage drop, $\mu_L = -\mu_R = eV$, and the wideband limit with constant DOS for the leads.

In Fig. 6, we show the semi-logarithmic (I–V) characteristic curves obtained using the DFT + DMFT total DOS for the different λ (main panel) and n (inset) values shown, respectively, in Figs. 3 and 4. As seen, γ-$CsPbI_3$ exhibits memristive behavior, where the resistance steady-state value

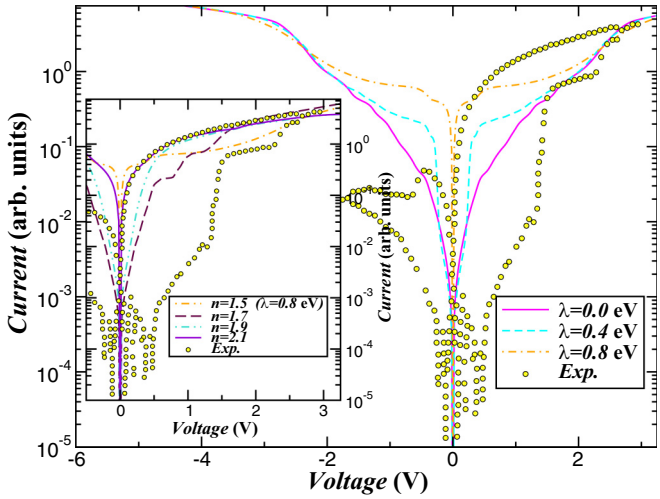

FIG. 6. Evolution of the semi-logarithmic (main panel) current-voltage (I–V) curves of γ-$CsPbI_3$ bulk crystal for different values of SOC (main panel) and total Pb-6p band filling (inset). Notice the memristive behavior with an ON/OFF ratio as high as 10^4 and the unipolar switching. In both panels, we displays a theory-experiment comparison of the I–V characteristics taken from Ref. [91], showing good qualitative agreement at positive voltages between experimental curve and the DFT + DMFT result for $n = 2.1$ in the inset.

shows an ON/OFF ratio as high as 10^4. Our results in Fig. 6 suggest that γ-$CsPbI_3$ exhibits resistive memory with unipolar (or symmetric) [95,96] low-resistance state (LRS) and high-resistance state (HRS). However, in contrast to the switching behavior derived within our theoretical framework, which does not depend on the polarity of the voltage and current signal, in experiments the I–V characteristic of γ-$CsPbI_3$ [91] is bipolar (or antisymmetric). This is because of the fact that the structure of the real system has some intrinsic asymmetry arising from different electrode materials or the voltage polarity during the initial electroforming step [95], resulting in a bipolar switching behavior.

To provide support to our correlated plus SOC and electron doping scenario, in Fig. 6 we compare our theoretical results with an experimental I–V curve taken from Ref. [91]. As seen, the experimental curve indicates that the sweep cycle of nonvolatile [97] devices is formed at positive and negative voltages, which may be mediated by the drift of ionic defects [91]. However, a particularly interesting feature observed in our results in the inset of Fig. 6 is the changes in selectivity as well as in the voltage window obtained for $n = 2.1$, suggesting that the changes in the I–V characteristics in experiment might also be influenced by the voltage dependence of the position of E_F relative to the top or the bottom of the valence and conduction band, as demonstrated in Ref. [82]. Importantly, both in theory (for $n = 2.1$) and experiment, during the applied voltage sweep from 3.0 V to 0 V the current decreases similarly. At this point, the system changes to a low-V chaotic [98] state, implying that the selector in experiment switches from an OFF state at 0.47 V to an ON state at 1.5 V and reaches a plateau, which almost coincides with our theory result for $n = 1.5$ near the border of the positive voltage loop. Thus, similar to other nonvolatile systems [99], after reaching the final current plateau at 3.0 V the current reduces as the applied voltage is swept back to the hold voltage, suggesting that γ-$CsPbI_3$ memristor changes its Pb-6p valence state, and the device returned to an OFF state at low voltages. Our results in the inset of Fig. 6, therefore, indicate that the small changes in the total Pb-6p band filling, resulting from doping or alloy engineering [80,81], are detrimental to inducing the memristive behavior in Pb-based perovskite for future neuromorphic computing.

III. CONCLUSIONS

In summary, we investigated the role of electron–electron interactions, SOC, and electron doping in shaping the MO Pb-6p electronic state of γ-$CsPbI_3$. Using the DFT + DMFT framework, we demonstrated that electronic correlations combined with SOC drive a profound reconstruction of the electronic structure, characterized by dynamical spectral weight transfer, a hallmark of correlated systems. Our results highlight the emergence of spin–orbit–induced bound states and their interplay with doping, which collectively leads to orbital-selective behavior and the onset of unconventional metallic phases. In a previously underrecognized correlated regime in γ-$CsPbI_3$, we show how SOC and electron correlations cooperate to generate in-gap resonances and orbital selectivity. Upon electron doping, γ-$CsPbI_3$ exhibits coexisting semiconducting and narrow bound states below the Fermi level, along with a doping-driven transition to a strange metal phase at critical band filling. These findings provide a microscopic description of the orbital-selective reconstruction in γ-$CsPbI_3$, positioning this compound as a model system for exploring the competition between MO electronic correlations, SOC, and doping in Pb-based halide perovskites.

ACKNOWLEDGMENTS

L.C.'s work is supported by CNPq (Grant No. 303359/2024-2). L.C. thanks FINEP (Project No. 0167/25). The work of B.O. is supported by CAPES. S.L. thanks the LeverhulmeTrust for support under Project No. RPG-2020-052, as well as ARCCA Cardiff for computational support.

DATA AVAILABILITY

The data that support the findings of this article are not publicly available upon publication because it is not technically feasible and/or the cost of preparing, depositing, and hosting the data would be prohibitive within the terms of this research project. The data are available from the authors upon reasonable request.

[1] A. Kojima, K. Teshima, Y. Shirai, and T. Miyasaka, Organometal halide perovskites as visible-light sensitizers for photovoltaic cells, J. Am. Chem. Soc. **131**, 6050 (2009).

[2] G. E. Eperon, M. T. Hörantner, and H. J. Snaith, Metal halide perovskite tandem and multiple-junction photovoltaics, Nat. Rev. Chem. **1**, 0095 (2017); G. M. Dalpian, X.-G. Zhao, L. Kazmerski, and A. Zunger, Formation and composition-dependent properties of alloys of cubic halide perovskites, Chem. Mater. **31**, 2497 (2019).

[3] N.-G. Park, Perovskite solar cells: An emerging photovoltaic technology, Mater. Today **18**, 65 (2015); Y. Rong, Y. Hu, A. Mei, H. Tan, M. I. Saidaminov, S. I. Seok, M. D. McGehee, E. H. Sargent, and H. Han, Challenges for commercializing perovskite solar cells, Science **361**, eaat8235 (2018); A. K. Jena, A. Kulkarni, and T. Miyasaka, Halide perovskite photovoltaics: Background, status, and future prospects Chem. Rev. **119**, 3036 (2019); J. Y. Kim, J.-W. Lee, H. S. Jung, H. Shin, and N.-G. Park, High-efficiency perovskite solar cells, *ibid.* **120**, 7867 (2020).

[4] A. Bouabça, A. Amar, H. Rozale, Y. Chrafih, and A. Chahed, Comprehensive DFT study of $CsXI_3$ (X = Pb, Sn) perovskites: structural, electronic, optical, and thermoelectric properties, J. Phys. Chem. Solids **208**, 113023 (2026).

[5] S. S. Ahmadi, P. Amiri, and H. Salehi, Structural, electronic, optical, and thermoelectric properties of $CsPbI_{3-y}Br_y$ (y = 0.5, 1.5, 2.5) compounds: First-principle study, J. Taiwan Inst. Chem. Engn. **155**, 105304 (2024).

[6] M. Saliba, T. Matsui, J.-Y. Seo, K. Domanski, J.-P. CorreaBaena, M. K. Nazeeruddin, S. M. Zakeeruddin, W. Tress, A. Abate, A. Hagfeldt, and M. Gratzel, Cesium-containing triple cation perovskite solar cells, Energy Environ. Sci. **9**, 1989 (2016).

[7] J. Liu, M. Wang, J. Lin, G. Chen, B. Liu, J. Huang, M. Zhang, G. Liang, L. Lu, P. Xu, B. Tian, H.-S. Kwokd, and G. Li, Mitigating deep-level defects through a self-healing process for highly efficient wide-bandgap inorganic $CsPbI_{3-x}Br_x$ perovskite photovoltaics, J. Mater. Chem. A **10**, 17237 (2022).

[8] S. Gharibzadeh, I. M. Hossain, P. Fassl, B. A. Nejand, T. Abzieher, M. Schultes, E. Ahlswede, P. Jackson, M. Powalla, S. Schäfer, *et al.*, 2D/3D heterostructure for semitransparent perovskite solar cells with engineered bandgap enables efficiencies exceeding 25% in four-terminal tandems with silicon and CIGS, Adv. Funct. Mater. **30**, 1909919 (2020); Y. Li, B. Shi, Q. Xu, L. Yan, N. Ren, Y. Chen, W. Han, Q. Huang, Y. Zhao, and X. Zhang, Wide bandgap interface layer induced stabilized perovskite/silicon tandem solar cells with stability over ten thousand hours, Adv. Energy Mater. **11**, 2102046 (2021).

[9] C. C. Stoumpos and M. G. Kanatzidis, The renaissance of halide perovskites and their evolution as emerging semiconductors, Acc. Chem. Res. **48**, 2791 (2015).

[10] C. C. Stoumpos, C. D. Malliakas, and M. G. Kanatzidis, Semiconducting tin and lead iodide perovskites with organic cations: Phase transitions, high mobilities, and near-infrared photoluminescent properties, Inorg. Chem. **52**, 9019 (2013); Q. Chen, N. D. Marco, Y. M. Yang, T.-B. Song, C.-C. Chen, H. Zhao, Z. Hong, H. Zhou, and Y. Yang, Under the spotlight: The organic–inorganic hybrid halide perovskite for optoelectronic applications, Nano Today **10**, 355 (2015).

[11] C. Gu and J.-S. Lee, Flexible hybrid organic–inorganic perovskite memory, ACS Nano **10**, 5413 (2016).

[12] B. Saparov and D. B. Mitzi, Organic–inorganic perovskites: Structural versatility for functional materials design, Chem. Rev. **116**, 4558 (2016).

[13] X. Zhang, X. Zhao, and Z. Wnag, Polyacrylonitrile passivation for enhancing the pptoelectronic switching performance of halide perovskite memristor for image Boolean logic applications, Nanomaterials **13**, 2174 (2023).

[14] Z. Xiao, Y. Yuan, Y. Shao, Q. Wang, Q. Dong, C. Bi, P. Sharma, A. Gruverman, and J. Huang, Giant switchable photovoltaic effect in organometal trihalide perovskite devices, Nat. Mater. **14**, 193 (2015).

[15] S. G., Y. Huang, X. Chen, X. Zhang, Z. Xiang, R. Zhang, W. Li, and Y. Cui, Silver iodide induced resistive switching in $CsPbI_3$ perovskite-based memory device, Adv. Mater. Interfaces **6**, 1802071 (2019); M. Loizos, K. Rogdakis, and E. Kymakis, Sustainable mixed-halide perovskite resistive switching memories using self-assembled monolayers as the bottom contact, J. Phys. Chem. Lett. **15**, 7635 (2024).

[16] J. S. Han, Q. V. Le, J. Choi, K. Hong, C. W. Moon, T. L. Kim, H. Kim, S. Y. Kim, and H. W. Jang, Air-stable cesium lead iodide perovskite for ultra-low perating voltage resistive switching, Adv. Funct. Mater. **28**, 1705783 (2017).

[17] Y. Yuan and J. Huang, Ion migration in organometal trihalide perovskite and its impact on photovoltaic efficiency and stabilty, Acc. Chem. Res. **49**, 286 (2016); G. Xia, B. Huang, Y. Zhang, X. Zhao, C. Wang, C. Jia, J. Zhao, W. Chen, and J. Li, Nanoscale insights into photovoltaic hysteresis in triple-cation mixed-halide perovskite: Resolving the role of polarization and ionic migration, Adv. Mater. **31**, 1902870 (2019).

[18] M. Loizos, K. Rogdakis, W. Luo, P. Zimmermann, A. Hinderhofer, J. Lukić, M. Tountas, F. Schreiber, J. V. Milić, and E. Kymakis, Resistive switching memories with enhanced durability enabled by mixed-dimensional perfluoroarene perovskite heterostructure, Nanoscale Horiz. **9**, 1146 (2024).

[19] M. H. Futscher and J. V. Milić, Mixed conductivity of hybrid halide perovskites: Emerging opportunities and challenges, Front. Energy Res. **9**, 629074 (2021).

[20] Z. Long, X. Qiu, C. L. J. Chan, Z. Sun, Z. Yuan, S. Poddar, Y. Zhang, Y. Ding, L. Gu, Y. Zhou, *et al.*, A neuromorphic bionic eye with filter-free color vision using hemispherical perovskite nanowire array retina, Nat. Commun. **14**, 1972 (2023).

[21] S. De Wolf, J. Holovsky, S. J. Moon, P. Löper, B. Niesen, M. Ledinsky, F. J. Haug, J. H. Yum, and C. Ballif, Organometallic halide perovskites: Sharp optical absorption edge and its relation to photovoltaic performance, J. Phys. Chem. Lett. **5**, 1035 (2014).

[22] H. Min, D. Y. Lee, J. Kim, G. Kim, K. S. Lee, J. Kim, M. J. Paik, Y. K. Kim, K. S. Kim, M. G. Kim, T. J. Shin, and S. Il Seok, Perovskite solar cells with atomically coherent interlayers on SnO_2 electrodes, Nature (London) **598**, 444 (2021).

[23] S. Y. Leblebici, L. Leppert, Y. Li, S. E. Reyes-Lillo, S. Wickenburg, E. Wong, J. Lee, M. Melli, D. Ziegler, D. K. Angell, and D. F. Ogletree, Facet-dependent photovoltaic efficiency variations in single grains of hybrid halide perovskite, Nat. Energy **1**, 16093 (2016).

[24] S. Tan, J. Shi, B. Yu, W. Zhao, Y. Li, Y. Li, H. Wu, Y. Luo, D. Li, and Q. Meng, Inorganic ammonium halide additive strategy for highly efficient and stable $CsPbI_3$ perovskite solar cells, Adv. Funct. Mater. **31**, 2010813 (2021).

[25] S. K. Radha, C. Bhandari, and W. R. L. Lambrecht, Distortion modes in halide perovskites: To twist or to stretch, a matter of tolerance and lone pairs, Phys. Rev. Mater. **2**, 063605 (2018).

[26] V. M. Goldschmidt, Die Gesetze der Krystallochemie, Naturwissenschaften **14**, 477 (1926).

[27] C. Yi, J. Luo, S. Meloni, A. Boziki, N. Ashari-Astani, C. Grätzel, S. M. Zakeeruddin, U. Rothlisberger, and M. Grätzel, Entropic stabilization of mixed A-cation ABX_3 metal halide perovskites for high performance perovskite solar cell, Energy Environ. Sci. **9**, 656 (2016).

[28] R. G. Niemann, L. Gouda, J. Hu, S. Tirosh, R. Gottesman, P. J. Cameron, and A. Zaban, Cs^+ incorporation into $CH_3NH_3PbI_3$ perovskite: substitution limit and stability enhancement, J. Mater. Chem. A **4**, 17819 (2016); W. Travis, E. N. K. Glover, H. Bronstein, D. O. Scanlon, and R. G. Palgrave, Nanoscale insights into photovoltaic hysteresis in triple-cation mixed-halide perovskite: Resolving the role of polarization and ionic migration, Chem. Sci. **7**, 4548 (2016).

[29] J. H. Noh, S. H. Im, J. H. Heo, T. N. Mandal, and S. I. Seok, Chemical management for colorful, efficient, and stable inorganic–organic hybrid nanostructured solar cells, Nano Lett. **13**, 1764 (2013); D. M. Jang, K. Park, D. H. Kim, J. Park, F. Shojaei, H. S. Kang, J.-P. Ahn, J. W. Lee, and J. K. Song, Reversible halide exchange reaction of organometal trihalide perovskite colloidal nanocrystals for full-range band gap tuning, *ibid.* **15**, 5191 (2015); Q. A. Akkerman, V. D' Innocenzo, S. Accornero, A. Scarpellini, A. Petrozza, M. Prato, and L. Manna, Tuning the optical properties of cesium lead halide perovskite nanocrystals by anion exchange reactions, J. Am. Chem. Soc. **137**, 10276 (2015); L. Protesescu, S. Yakunin, M. I. Bodnarchuk, F. Krieg, R. Caputo, C. H. Hendon, R. X. Yang, A. Walsh, and M. V. Kovalenko, Nanocrystals of cesium lead halide perovskites ($CsPbX_3$, X = Cl, Br, and I): Novel optoelectronic materials showing bright emission with wide color gamut, Nano Lett. **15**, 3692 (2015).

[30] J. B. Bechtel and A. Van der Ven, First-principles thermodynamics study of phase stability in inorganic halide perovskite solid solutions, Phys. Rev. Mater. **2**, 045401 (2018).

[31] A. M. Glazer, The classification of tilted octahedra in perovskites, Acta Crystallogr. B Struct. Crystallogr. Cryst. Chem. **28**, 3384 (1972).

[32] J. S. Bechtel and A. V. der Ven, Octahedral tilting instabilities in inorganic halide perovskites, Phys. Rev. Mater. **2**, 025401 (2018).

[33] D. E. Scaife, P. F. Weller, and W. G. Fisher, Crystal preparation and properties of cesium tin(II) trihalides, J. Solid State Chem. **9**, 308 (1974).

[34] K. Yamada, S. Funabiki, H. Horimoto, T. Matsui, T. Okuda, and S. Ichiba, Structural phase transitions of the polymorphs of $CsSnI_3$ by means of rietveld analysis of the x-ray diffraction, Chem. Lett. **801**, 20 (1991).

[35] E. L. da Silva, J. M. Skelton, S. C. Parker, and A. Walsh, Phase stability and transformations in the halide perovskite $CsSnI_3$, Phys. Rev. B **91**, 144107 (2015).

[36] I. Chung, J.-H. Song, J. Im, J. Androulakis, C. D. Malliakas, H. Li, A. J. Freeman, J. T. Kenney, and M. G. Kanatzidis, $CsSnI_3$: Semiconductor or metal? High electrical conductivity and strong near-infrared photoluminescence from a single material. High hole mobility and phase-transitions, J. Am. Chem. Soc. **134**, 8579 (2012).

[37] C. K. Moeller, Crystal structure and photoconductivity of Cæsium plumbohalides, Nature (London) **182**, 1436 (1958).

[38] C.-K. Lin, Y. Zhang, M. Gao, J.-A. Lin, H. K. D. Le, Z. Lin, and P. Yang, Controlling the phase transition in $CsPbI_3$ nanowires, Nano Lett. **22**, 2437 (2022).

[39] D. P. McMeekin, G. Sadoughi, W. Rehman, G. E. Eperon, M. Saliba, M. T. Hörantner, A. Haghighirad, N. Sakai, L. Korte, B. Rech, *et al.*, A mixed-cation lead mixed-halide perovskite absorber for tandem solar cells, Science **351**, 151 (2016); H. Choi, J. Jeong, H.-B. Kim, S. Kim, B. Walker, G.-H. Kim, and J. Y. Kim, Cesium-doped methylammonium lead iodide perovskite light absorber for hybrid solar cells, Nano Energy **7**, 80 (2014); J.-W. Lee, D.-H. Kim, H.-S. Kim, S.-W. Seo, S. M. Cho, and N.-G. Park, Formamidinium and cesium hybridization for photo- and moisture-stable perovskite solar cell, Adv. Energy Mater. **5**, 1501310 (2015); Z. Li, M. Yang, J.-S. Park, S.-H. Wei, J. J. Berry, and K. Zhu, Stabilizing perovskite structures by tuning tolerance factor: Formation of formamidinium and cesium lead iodide solid-state alloys, Chem. Mater. **28**, 284 (2016).

[40] D. M. Trots and S. V. Myagkota, High-temperature structural evolution of caesium and rubidium triiodoplumbates, J. Phys. Chem. Solids **69**, 2520 (2008).

[41] A. Marronnier, G. Roma, S. Boyer-Richard, L. Pedesseau, J. M. Jancu, Y. Bonnassieux, C. Katan, C. C. Stoumpos, M. G. Kanatzidis, and J. Even, Anharmonicity and disorder in the black phases of cesium lead iodide used for stable inorganic perovskite solar cells, ACS Nano **12**, 3477 (2018).

[42] G. E. Eperon, S. D. Stranks, C. Menelaou, M. B. Johnston, L. M. Herz, and H. J. Snaith, Formamidinium lead trihalide: A broadly tunable perovskite for efficient planar heterojunction solar cells, Energy Environ. Sci. **7**, 982 (2014).

[43] Y. Wang, T. Zhang, M. Kan, and Y. Zhao, Bifunctional stabilization of all-inorganic α-CsPbI3 perovskite for 17% efficiency photovoltaics, J. Am. Chem. Soc. **140**, 12345 (2018).

[44] Y. Wang, M. I. Dar, L. K. Ono, T. Zhang, M. Kan, Y. Li, L. Zhang, X. Wang, Y. Yang, X. Gao, *et al.*, Thermodynamically stabilized β-$CsPbI_3$–based perovskite solar cells with efficiencies >18%, Science **365**, 591 (2019).

[45] B. Zhao, S.-F. Jin, S. Huang, N. Liu, J.-Y. Ma, D.-J. Xue, Q. Han, J. Ding, Q.-Q. Ge, Y. Feng, J.-S. Hu, Thermodynamically stable orthorhombic γ-$CsPbI_3$ thin films for high-performance photovoltaics, J. Am. Chem. Soc. **140**, 11716 (2018).

[46] R. J. Sutton, M. R. Filip, A. A. Haghighirad, N. Sakai, B. Wenger, F. Giustino, and H. J. Snaith, Cubic or orthorhombic? Revealing the crystal structure of metastable black-phase $CsPbI_3$ by theory and experiment, ACS Energy Lett. **3**, 1787 (2018).

[47] A. Morronnier, G. Roma, M. Carignano, Y. Bonnassieux, C. Katan, J. Even, E. Mosconi, and F. De Angelis, Influence of disorder and anharmonic fluctuations on the dynamical Rashba effect of purely inorganic lead-halide perovskite, J. Phys. Chem. C **123**, 291 (2018).

[48] F. Brivio, K. T. Butler, A. Walsh, and M. van Schilfgaarde, Relativistic quasiparticle self-consistent electronic structure of hybrid halide perovskite photovoltaic absorbers, Phys. Rev. B **89**, 155204 (2014).

[49] C. M. O. Bastos, F. P. Sabino, G. M. Sipahi, J. L. F. Da Silva, A comprehensive study of g-factors, elastic, structural and

electronic properties of III-V semiconductors using hybrid-density functional theory, J. Appl. Phys. **123**, 065702 (2018).

[50] M. R. Filip and F. Giustino, *GW* quasiparticle band gap of the hybrid organic-inorganic perovskite $CH_3NH_3PbI_3$: Effect of spin-orbit interaction, semicore electrons, and self-consistency, Phys. Rev. B **90**, 245145 (2014); C.-J. Yu, U.-H. Ko, S.-G. Hwang, Y.-S. Kim, U.-G. Jong, Y.-H. Kye, and C.-H. Ri, First-principles study on material properties and stability of inorganic halide perovskite solid solutions $CsPbI(I_{1-x}Br_x)_3$, Phys. Rev. Mater. **4**, 045402 (2020); J. Yang, T. Zhu, and S. Liu, Onsite and intersite electronic correlations in the Hubbard model for halide perovskites, Phys. Rev. B **106**, 195159 (2022).

[51] L. Craco and S. S. Carara, Atomic many-body selectivity in cubic $CsPbI_3$ solar cell memristor, Compounds **5**, 7 (2025).

[52] L. Craco and S. Leoni, Magnetoresistance in the spin-orbit Kondo state of elemental bismuth, Sci. Rep. **5**, 13772 (2015).

[53] L. Craco and S. Leoni, Bulk quantum correlations and doping-induced nonmetallicity in the Bi_2Se_3 topological insulator, Phys. Rev. B **85**, 075114 (2012); Tunable Kondo-Mott physics in bulk Bi_2Te_2Se topological insulator, **85**, 195124 (2012); L. Craco, On-site electron correlations in Bi_2Se_3 topological insulator, Eur. Phys. J. B **88**, 292 (2015).

[54] B. Amadon, First-principles DFT DMFT calculations of structural properties of actinides: Role of Hund's exchange, spin-orbit coupling, and crystal structure, Phys. Rev. B **94**, 115148 (2016); J. I. Facio, J. Mravlje, L. Pourovskii, P. S. Cornaglia, and V. Vildosola, Spin-orbit and anisotropic strain effects on the electronic correlations in Sr_2RuO_4, *ibid.* **98**, 085121 (2018); A. J. Kim, P. Werner, and R. Valentí, Alleviating the sign problem in quantum Monte Carlo simulations of spin-orbit-coupled multiorbital Hubbard models, *ibid.* **101**, 045108 (2020).

[55] F. P. Sabino, X. G. Zhao, G. M. Dalpian, and A. Zunger, Impact of symmetry breaking and spin-orbit coupling on the band gap of halide perovskites, Phys. Rev. B **110**, 035160 (2024).

[56] M. Hirasawa, T. Ishihara, and T. Goto, Exciton features in 0-, 2-, and 3-dimensional networks of $[PbI_{6_4}]$-octahedra, J. Phys. Soc. Jpn. **63**, 3870 (1994).

[57] J. Brgoch, A. J. Lehner, M. Chabinyc, and R. Seshadri, *Ab initio* calculations of band gaps and absolute band positions of polymorphs of $RbPbI_3$ and $CsPbI_3$: Implications for main-group halide perovskite photovoltaics, J. Phys. Chem. C **118**, 27721 (2014).

[58] A. Amat, E. Mosconi, E. Ronca, C. Quarti, P. Umari, M. K. Nazeeruddin, M. Grätzel, and F. De Angelis, Cation-induced band-gap tuning in organohalide perovskites: Interplay of spin-orbit coupling and octahedra tilting, Nano Lett. **14**, 3608 (2014).

[59] J. Even, L. Pedesseau, J.-M. Jancu, and C. Katan, Importance of spin-orbit coupling in hybrid organic/IInorganic perovskites for photovoltaic applications, J. Phys. Chem. Lett. **4**, 2999 (2013).

[60] Z. Wang, O. I. Malyi, X. Zhao, and A. Zunger, Mass enhancement in 3*d* and *s*–*p* perovskites from symmetry breaking, Phys. Rev. B **103**, 165110 (2021).

[61] M. Hussain, M. Rashid, F. Saeed, and A. S. Bhatti, Spin–orbit coupling effect on energy level splitting and band structure inversion in $CsPbBr_3$, J. Mater. Sci. **56**, 528 (2021).

[62] D. Liu, Z. Shao, C. Li, S. Pang, Y. Yan. and G. Cui, Structural properties and stabilitiy of inorganic $CsPbI_3$ perovskites, Small Struct. **2**, 2000089 (2021).

[63] U.-G. Jong, C.-J. Yu, Y.-S. Kim, Y.-H. Kye, and C.-H. Kim, First-principles study on the material properties of the inorganic perovskite $Rb_{1-x}Cs_xPbI_3$ for solar cell applications, Phys. Rev. B **98**, 125116 (2018).

[64] G. Kotliar, S. Y. Savrasov, K. Haule, V. S. Oudovenko, O. Parcollet, and C. A. Marianetti, Electronic structure calculations with dynamical mean-field theory, Rev. Mod. Phys. **78**, 865 (2006).

[65] Y. Tada, R. Peters, M. Oshikawa, A. Koga, N. Kawakami, and S. Fujimoto, Correlation effects in two-dimensional topological insulators, Phys. Rev. B **85**, 165138 (2012).

[66] D. Calugaru, H. Hu, L. Crippa, G. Rai, N. Regnault, T. O. Wehling, R. Valentí, G. Sangiovanni, and B. A. Bernevig, Obtaining the spectral function of moiré graphene heavy-fermions using iterative perturbation theory, arXiv:2509.18256.

[67] J. M. Soler, E. Artacho, J. D. Gale, A. García, J. Junquera, P. Ordejón, and D. Sánchez-Portal, The SIESTA method for *ab initio* order-N materials simulation, J. Phys.: Condens. Matter **14**, 2745 (2002).

[68] J. P. Perdew, K. Burke, and M. Ernzerhof, Generalized gradient approximation made simple, Phys. Rev. Lett. **77**, 3865 (1996).

[69] H. J. Monkhorst and J. D. Pack, Special points for Brillouin-zone integrations, Phys. Rev. B **13**, 5188 (1976).

[70] N. Marzari, A. A. Mostofi, J. R. Yates, I. Souza, and D. Vanderbilt, Maximally localized Wannier functions: Theory and applications, Rev. Mod. Phys. **84**, 1419 (2012); G. Pizzi, V. Vitale, R. Arita, S. Blëgel, F. Freimuth, G. Géranton, M. Gibertini, D. Gresch, C. Johnson, T. Koretsune, *et al.*, Wannier90 as a community code: New features and applications, J. Phys.: Condens. Matter **32**, 165902 (2020).

[71] M. S. Hybertsen and S. G. Louie, Electron correlation in semiconductors and insulators: Band gaps and quasiparticle energies, Phys. Rev. B **34**, 5390 (1986); M. F. Pereira Jr and K. Henneberger, Microscopic theory for the optical properties of Coulomb-correlated semiconductors, Phys. Stat. Sol. (b) **206**, 477 (1998); D. S. Chemla and J. Shah, Many-body and correlation effects in semiconductors, Nature (London) **411**, 549 (2001); A. Galler, J. Boust, A. Demourgues, S. Biermann, and L. V. Pourovskii, Correlated electronic structure and optical response of rare-earth based semiconductors, Phys. Rev. B **103**, L241105 (2021); D. V. Tuan, H. Dery, Excitons and trions in monolayer semiconductors with correlated electrons, *ibid.* **108**, 085303 (2023); V. Christiansson, F. Petocchi, P. Werner, Self-consistent GW+EDMFT for semiconductors and insulators, arXiv:2410.19579.

[72] S. Fujimoto, Topological order and non-Abelian statistics in noncentrosymmetric *s*-wave superconductors, Phys. Rev. B **77**, 220501(R) (2008); S.-L. Yu, X. C. Xie, and J.-X. Li, Mott physics and topological phase transition in correlated Dirac fermions, Phys. Rev. Lett. **107**, 010401 (2011).

[73] L. Craco, Insulator-to-metal crossover induced by local spin fluctuations in strongly correlated systems, J. Phys.: Condens. Matter **13**, 263 (2001).

[74] N.-O. Linden, M. Zingl, C. Hubig, O. Parcollet, and U. Schollwöck, Imaginary-time matrix product state impurity solver in a real material calculation: Spin-orbit coupling in Sr_2RuO_4, Phys. Rev. B **101**, 041101(R) (2020); M. E. Merkel, A. M. Tehrani, and C. Ederer, Probing the Mott insulating behavior of Ba_2 $MgReO_6$ with DFT+DMFT, Phys. Rev. Res. **6**, 023233 (2024); F. Sorgenfrei, M. Alouani, J. Schött, H. J. M.

Jönsson, O. Eriksson, and P. Thunström, Theory of x-ray absorption spectroscopy for ferrites, Phys. Rev. B **109**, 115126 (2024).

[75] L. Craco, Quantum orbital entanglement: A view from the extended periodic Anderson model, Phys. Rev. B **77**, 125122 (2008).

[76] Smaller U values will induce rather small correlation effects on the Pb − 6p states of −$CsPbI_3$ because of its intrinsically large one-particle bandwidth, W.

[77] B. Freelon, Y. H. Liu, J.-L . Chen, L. Craco, M. S. Laad, S. Leoni, J. Chen, L. Tao, H. Wang, R. Flauca, Z. Yamani, M. Fang, C. Chang, J.-H . Guo, Z. Hussain, Mott-Kondo insulator behavior in the iron oxychalcogenides, Phys. Rev. B **92**, 155139 (2015).

[78] R. Martin and J. Allen, Theory of mixed valence: Metals or small gap insulators, J. Appl. Phys. **50**, 7561 (1979).

[79] M. Dzero, K. Sun, V. Galitski, and P. Coleman, Topological Kondo insulators, Phys. Rev. Lett. **104**, 106408 (2010).

[80] B. Jiang, X. Chen, X. Pan, L. Tao, Y. Huang, J. Tang, X. Li, P. Wang, G. Ma, J. Zhang, and H. Wang, Advances in metal halide perovskite memristors: A review from a Co-design perspective, Adv. Sci. **12**, 2409291 (2024).

[81] M. T. Weller, O. J. Weber, J. M. Frost, and A. Walsh, Cubic perovskite structure of black formamidinium lead iodide, α-$[HC(NH_2)_2]PbI_3$, at 298 K, J. Phys. Chem. Lett. **6**, 3209 (2015); T. J. Whitcher, J.-X. Zhu, X. Chi, H. Hu, D. Zhao, T. C. Asmara, X. Yu, M. B. H. Breese, A. H. Castro Neto, Y. M. Lam, A. T. S. Wee, E. E. M. Chia, and A. Rusydi, Importance of electronic correlations and unusual excitonic effects in formamidinium lead halide perovskites, Phys. Rev. X **8**, 021034 (2018); J. Park, K. M. Griffith, and Y. Duan, Systematic characterization on optical and phonon properties of $Cs[Pb_xSn_{1-x}]I_3$ alloyed perovskites via first-principles modeling, J. Phys. Chem. C **126**, 8832 (2022); L. O. de Araujo, C. R. C. Rêgo, W. Wenzel, D. N. Silveira, M. J. Piotrowski, F. P. Sabino, Y. Pramudya, and D. Guedes-Sobrinho, How cation nature controls the bandgap and bulk Rashba splitting of halide perovskites, J Comput. Chem. **44**, 1395 (2023).

[82] C.-P. Lu, G. Li, J. Mao, L.-M. Wang, and E. Y. Andrei, Bandgap, mid-gap states, and gating effects in MoS_2, Nano Lett. **14**, 4628 (2014).

[83] E. E. Salpeter and H. A. Bethe, A relativistic equation for bound-state problems, Phys. Rev. **84**, 1232 (1951).

[84] W. Qi, S. Ponzoni, G. Huitric, V. Gorelov, A. Pramanik, Y. Laplace, M. Marsi, E. Papalazarou, S. F. Maehrlein, E. Deleporte, *et al.*, About Carrier's self-trapping and dynamical Rashba splitting in the two-dimensional hybrid perovskite $(BA)_2(MA)_2Pb_3I_{10}$, arXiv:2508.12129.

[85] K. Haule and G. Kotliar, Coherence–incoherence crossover in the normal state of iron oxypnictides and importance of Hund's rule coupling, New J. Phys. **11**, 025021 (2009).

[86] C. Grenzebach, F. B. Anders, and G. Czycholl, Transport properties of heavy-Fermion systems, Phys. Rev. B **74**, 195119 (2006).

[87] K. Urasaki and T. Saso, Correlation effects on optical conductivity of FeSi, J. Phys. Soc. Jpn. **68**, 3477 (1999); T. Saso, Calculation of optical conductivity of YbB12 using realistic tight-binding model *ibid.* **73**, 2894 (2004).

[88] L. Baldassarre, A. Perucchi, D. Nicoletti, A. Toschi, G. Sangiovanni, K. Held, M. Capone, M. Ortolani, L. Malavasi, M. Marsi, P. Metcalf, P. Postorino, and S. Lupi, Quasiparticle evolution and pseudogap formation in V_2O_3: An infrared spectroscopy study, Phys. Rev. B **77**, 113107 (2008); M. S. Laad, L. Craco, S. Leoni, and H. Rosner, Electrodynamic response of incoherent metals: Normal phase of iron pnictides, *ibid.* **79**, 024515 (2009).

[89] L. Craco and M. S. Laad, Normal state incoherent pseudogap in FeSe superconductor, Eur. Phys. J. B **89**, 119 (2016); L. Craco, T. A. da Silva Pereira, and S. Leoni, Electronic structure and thermoelectric transport of black phosphorus, Phys. Rev. B **96**, 075118 (2017); L. Craco and S. Leoni, Effect of localization–delocalization transition on thermoelectric properties of Bi_2Te_2Se topological insulator, APL Energy **2**, 016102 (2024).

[90] K. Zhang, G. Chen, and S. Jia, Spin-orbit-induced bound state and molecular signature of the degenerate Fermi gas in a narrow Feshbach resonance, Phys. Rev. A **88**, 013611 (2013); X. Zhao, J. Wang, W. Liu, Z. Che, X. Wang, C. T. Chan, L. Shi, and J. Zi, Spin-orbit-locking chiral bound states in the continuum, Phys. Rev. Lett. **133**, 036201 (2024).

[91] L. Xu, Y. Fu, Y. Li, G. Zhou, and X. Lu, $CsPbI_3$ perovskite quantum dot-based worm memory device with intrinsic ternary states, ACS Appl. Mater. Interfaces **16**, 39827 (2024).

[92] Y. Meir and N. S. Wingreen, Landauer formula for the current through an interacting electron region, Phys. Rev. Lett. **68**, 2512 (1992).

[93] L. Craco and K. Kang, Perturbation treatment for transport through a quantum dot, Phys. Rev. B **59**, 12244 (1999).

[94] G. Cuniberti, L. Craco, D. Porath, and C. Dekker, Backbone-induced semiconducting behavior in short DNA wires, Phys. Rev. B **65**, 241314(R) (2002); X.-X. Bao and X.-F. Wang, Effects of long-range dispersive interaction on the electron transport in short single strands of guanine bases, Int. J. Quantum Chem. **124**, e27251 (2023).

[95] R. Waser and M. Aono, Nanoionics-based resistive switching memories, Nat. Mater. **6**, 833 (2007).

[96] A. Chen, Y. Fu, G. Yang, N. Liu, X. Zhao, Z. Zhang, L. Tao, H. Wan, Y. Rao, J. Duan, *et al.*, The Co-improvement of selectivity and uniformity on NbO_x-based selector by Al-doping, IEEE Electron Device Lett. **43**, 870 (2022).

[97] R. Wang, J.-Q. Yang, J.-Y. Mao, Z.-P. Wang, S. Wu, M. Zhou, T. Chen, Y. Zhou, and S.-T. Han, Recent advances of volatile memristors: devices, mechanisms, and applications, Adv. Intell. Syst. **2**, 202000055 (2020); V. K Sangwan and M. C. Hersam, Neuromorphic nanoelectronic materials, Nat. Nanotechnol. **15**, 517 (2020).

[98] See for example, S. Kumar, J. P. Strachan, R. S. Williams, Chaotic dynamics in nanoscale NbO_2 Mott memristors for analog, Nature (London) **548**, 318 (2017); M. Escudero, S. Spiga, and S. Brivio, Memristive chaotic circuit for information processing through time, Adv. Intell. Syst. **8**, 2500508 (2025).

[99] M.-K. Song, J.-H. Kang, X. Zhang, W. Ji, A. Ascoli, I. Messaris, A. S. Demirkol, B. Dong, S. Aggarwal, W. Wan, and S.-M. Hong, Recent advances and future prospects for memristive materials, devices, and systems, ACS Nano **17**, 11994 (2023); Y. Ran, Y. Pei, Z. Zhou, H. Wang, Y. Sun, Z. Wang, M. Hao, J. Zhao, J. Chen, and X. Yan, A review of Mott insulator in memristors: The materials, characteristics, applications for future computing systems and neuromorphic computing, Nano Res. **16**, 1165 (2023).